

FINAL TECHNICAL REPORT

FOR

AFOSR Grant # F49620-93-1-0016

AFOSR Program Manager
Stanley K. Dickinson
AFOSR/NL
Building 410
Bolling AFB, DC 20332-6448

**DISCRIMINATING UNDERGROUND EXPLOSIONS FROM EARTHQUAKES
 USING SEISMIC CODA WAVES**

Principal Investigator

Keiiti Aki
Department of Earth Sciences
University of Southern California
Los Angeles, California 90089-0740
213-740-5830
213-740-0011 (fax)
aki@coda.usc.edu

Accesion For	
NTIS	CRA&I <input checked="" type="checkbox"/>
DTIC	TAB <input type="checkbox"/>
Unannounced <input type="checkbox"/>	
Justification _____	
By _____	
Distribution / _____	
Availability Codes	
Dist	Avail and / or Special
A-1	

Participating Scientists

Xiaofei Chen, Anshu Jin and Feng Su
Department of Earth Sciences
University of Southern California
Los Angeles, CA 90089-0740

DTIC QUALITY INSPECTED 4

January, 1995

19950214 021

REPORT DOCUMENTATION PAGE

Form Approved
OMB No. 0704-0188

Public reporting burden for this collection of information is estimated to average 1 hour per response, including the time for reviewing instructions, searching existing data sources, gathering and maintaining the data needed, and completing and reviewing the collection of information, including suggestions for reducing this burden. Send comments regarding this burden estimate or any other aspect of this collection of information, including suggestions for reducing this burden, to Washington Headquarters Services, Directorate for Information Operations and Reports, 1215 Jefferson Davis Highway, Suite 1204, Arlington, VA 22202-4302, and to the Office of Management and Budget, Paperwork Reduction Project (0704-0188), Washington, DC 20503.

TABLE OF CONTENTS

SUMMARY	1
1. INTRODUCTION	1
2. SEISMIC CODA WAVE DISCRIMINATION METHOD FOR LOCAL EVENTS AND ITS APPLICATION TO QUARRY BLAST - EARTHQUAKE DISCRIMINATION	
2.1 The Method	3
2.2 The Result of Discrimination Quarry Blasts from Earthquakes	4
3. SEISMIC SCATTERING THEORY FOR SURFACE WAVES AND BODY WAVES AND ITS IMPLICATION OF DISCRIMINATION OF EXPLOSION- EARTHQUAKE AT REGIONAL DISTANCE	7
3.1 Energy Transfer Theory for Rayleigh Wave	8
3.2 Energy Transfer Theory for S and Rayleigh Waves' Scattering Processes	12
3.3 Discussion on the Discrimination of Earthquakes and Explosions at Regional Distance	15
4. DISCUSSIONS AND CONCLUSIONS	16
REFERENCES	17

SUMMARY

We have successfully discriminated the quarry blasts and earthquakes at local distance from the observed source power spectra by using the coda Q method. To extend this discrimination method to the events at regional distances, we have developed the energy transfer theory for a mixture of Rayleigh and S wave propagation in a random scattering and attenuation medium. Applying this theory to the quarry blast-earthquake problem at local distance, we can explain the observations satisfactorily. Our study indicates that the Rayleigh waves' scattering become important for the events with shallower focal depth such as the quarry blasts and nuclear explosions. By fitting our theoretical attenuation curves to the observed ones at local distances, we have obtained the S and Rayleigh waves' intrinsic and scattering coefficients, and the coupled scattering coefficient of Rayleigh with S waves. Assuming that these coefficients are valid for the events at regional distances, we have compared the predicted and observed coda envelope at regional distances for the purpose of discrimination between the earthquakes and explosions at regional distance. Our prediction shows that the Rayleigh wave's contributions become more significant for shallower events (explosions), while for deeper events (earthquakes) the Rayleigh wave's contributions are still negligible. Comparison between predicted and the data of CDSN suggests that the discrimination of earthquakes and explosions at regional distance may be possible by using the coda method for the high frequency case. For the low frequency case, we must consider the crustal effects.

1. INTRODUCTION

Numerous studies on discrimination between underground explosions and earthquakes at regional distances during the last decade have been based on variations of spectral characteristics of direct wave phases (Pn, Pg, Lg, Rg, etc.) or on spectral ratios between different frequencies. Explosions and earthquakes have yielded different spectral amplitudes for the same direct wave phase at regional distances in many cases (e.g., Murphy and Bennett, 1982; Pomeroy et al., 1982; Bennett and Murphy, 1986; Bennett et al., 1989; Smith, 1989) and can be used to discriminate underground explosions from earthquakes. Since these direct waves are strongly affected by a particular source-receiver path, determining whether the observed differences in these direct signals are due to the source or propagation path effect can be difficult, especially when the locations of the explosions and earthquakes are not close. Furthermore, the late

P coda waves, direct S wave and surface waves are usually mixed together, and it is difficult to isolate individual wave phases.

The above problems can be solved using the coda wave method (Aki and Chouet, 1975). The fundamental characteristic of coda waves is that its decay depends on the average properties of the region surrounding the source and station, independent of any particular wave path. This property allows us to isolate the source effect from path effects, compare source differences between explosions and earthquakes, and develop a reliable discrimination method.

According to the above idea, we developed a seismic coda wave discrimination method and succeeded in applying it to discriminate quarry blasts from earthquakes at local distance in an area encompassing the south-central Mojave Desert and Eastern Transverse Ranges in Southern California. We found that the coda decay rate Q_c^{-1} is significantly higher for quarry blasts than earthquakes for lower frequencies ($f < 6$ Hz) for lapse time up to about 30 sec. This result is attributed to the greater contribution of surface waves to quarry blasts due to their shallow source depth. The difference in Q_c^{-1} , however, disappears for lapse time greater than 30 sec for the same frequency range as well as for higher frequencies ($f \geq 6$ Hz) for lapse time greater than 20 sec, suggesting that the coda waves at high frequencies, or at low frequencies for late lapse time, are dominated by the same body waves, probably S waves, for both quarry blasts and earthquakes. The coda power spectrum (after correction of path attenuation) of the quarry blasts is significantly different from that of the earthquakes. The curves of coda power spectra versus frequency for quarry blasts decrease more sharply than earthquakes at high frequencies, indicating a lack of energy in high frequencies for quarry blast sources as compared to earthquake sources. The different frequency dependence of coda power spectra between quarry blasts and earthquakes is attributed to their different source properties and can be used for seismic discrimination.

To extend this idea to the seismic discrimination of explosions and earthquakes at regional distances, we need to interpret the scattering properties of body waves mixed with surface waves. We shall first develop a theory for surface waves scattering and coupling with body wave. Using this theory we shall investigate the possibility of the seismic discrimination of explosions and earthquakes at regional distance.

2. SEISMIC CODA WAVE DISCRIMINATION METHOD FOR LOCAL EVENTS AND ITS APPLICATION TO QUARRY BLAST-EARTHQUAKE DISCRIMINATION.

2.1 The Method

Generally, the observed coda wave decay rate is very stable, independent of source-receiver location, whereas the absolute amplitude of the coda waves is dependent on source and site (Aki, 1969; Aki and Chouet, 1975). The power spectrum of the coda wave $P(\omega|t)$ can be considered as a product of three factors:

$$P(\omega|t) = \text{source}(\omega) \cdot \text{site}(\omega) \cdot \text{path}(\omega|t), \quad (1)$$

where ω is the circular frequency and t is the lapse time measured from the event origin time. Using the first order body wave scattering model of the coda waves (Aki and Chouet, 1975; Zeng et al., 1990), the above equation can be written explicitly as

$$\ln[P(\omega|t)t^2] = C(\omega) - \omega Q_c^{-1}t, \quad (2)$$

where $C(\omega)$ is determined by the source and site effects at a given ω . Q_c^{-1} is a parameter measuring the coda wave decay rate.

Since the first order scattering model neglects the higher order multiple scattering, it is not surprising that the linear relationship expressed in Equation (2) holds well for only a finite range of lapse time. We observed the coda decay rates decreasing gradually with increasing lapse time. In order to incorporate the lapse time dependent coda Q_c^{-1} , we define it by the following equation:

$$\frac{\partial}{\partial t} \left\{ \ln[P(\omega|t)t^2] \right\} = -\omega Q_c^{-1}(\omega, t), \quad (3)$$

where $Q_c^{-1}(\omega, t)$ was determined by a moving lapse time window (centered at t) in the data processing. In order to find the expression for $P(\omega|t)$ by integrating Equation (3), it is necessary to introduce a reference time t_r . As can be seen later when we show the observed Q_c^{-1} as a function of t , we shall find that Q_c^{-1} becomes approximately constant for t greater than a certain time, which depends on frequency. It is then convenient to define the time beyond which $Q_c^{-1}(\omega, t)$ becomes constant as the reference time t_r . The integration of Equation (3) from t_r to t ($t_r \geq t$) gives rise to

$$P(\omega|t_r)t_r^2 \exp(\omega Q_{C_r}^{-1}t_r) = P(\omega|t)t^2 \exp(\omega Q_c^{-1}t) \quad (t \geq t_r) \quad (4)$$

where $Q_{C_r}^{-1}$ represents constant Q_c^{-1} after time t_r . Equation (4) shows that $P(\omega|t_r)t_r^2 \exp(\omega Q_{C_r}^{-1}t_r)$, $t \geq t_r$, is a constant for a given frequency. The physical meaning of the constant is clear - it is the coda power spectrum corrected for geometrical spreading and attenuation back to the origin time. We define

$$P_o(\omega) = P(\omega|t)t^2 \exp(\omega Q_c^{-1}t) \quad (t \geq t_r) \quad (5)$$

Obviously, the power spectrum $P_o(\omega)$ we defined in Equation (5) is not only controlled by the source, but is also affected by the recording site. If we compare the power spectrum $P_o(\omega)$ of quarry blasts and earthquakes at the same station, however, the difference between them should be attributed to the source effect only. Integrating Equation (3) again from an observation time t to the reference time t_r , we find

$$\ln[P(\omega|t_r)t_r^2] - \ln[P(\omega|t)t^2] = -\omega \int_t^{t_r} Q_c^{-1}(\omega, t) dt. \quad (6)$$

Combining Equations (5) and (6), we obtain

$$\ln[P_o(\omega)] = \ln[P(\omega|t)t^2] + \omega Q_{C_r}^{-1}t_r - \omega \int_t^{t_r} Q_c^{-1}(\omega, t) dt \quad (7)$$

Formula (7) is obtained under the assumption that $Q_c^{-1}(\omega, t)$ is independent of t for $t \geq t_r$. For the purpose of the comparison of the coda source power spectra between explosions and earthquakes, it can be generalized to the case in which the coda decay of explosions and earthquakes are the same (instead of the same constant Q_c^{-1} after t_r).

2.2 The Result of Discrimination Quarry Blasts from Earthquakes

A total of 58 earthquake and 48 quarry blasts distributed in an area encompassing the south central Mojave Desert and Eastern Transverse Range (Figure 1) were used for this study. These events were recorded from 1981 to 1987 by the USGS-CALTECH Southern California seismograph network. The quarries are operated by the Southwestern Portland Cement Company. The blasting practice during this period was by single instantaneous shot in holes at depths of about 35 feet (J. Stafford, personal communication, 1990). The earthquake focal depths range from 0 to 12 km and their magnitudes range from 2.1 to 3.5.

Data from both quarry blast and earthquake sources were processed by an identical procedure to study the possible differences in coda attenuation. Figures 2a through 2d show the measured Q_c^{-1} of earthquake plotted as a function of lapse time for frequencies 1.5, 3.0, 6.0, and 12.0 Hz, respectively, while Figure 2a through 2h show the corresponding results for quarry blasts. Each small open circle on the plots represents one measurement for a particular seismogram with a moving lapse time window of fixed width, which is 34 sec for frequency 1.5 Hz, 25 sec for 3.0 Hz, and 20 sec for 6.0 and 12.0 Hz. The resultant Q_c^{-1} values for all earthquakes were plotted together. The solid lines connect the mean points (solid circles) calculated by averaging the individual measurements in each 8 sec time interval with 4 sec overlapping at the adjacent mean points. The standard error of the mean is also shown for each mean point.

From the comparison of Figures 2a through 2h, we find a significant difference in Q_c^{-1} between quarry blasts and earthquakes for the lower frequencies of 1.5 and 3 Hz for lapse times less than 30 sec. this difference in Q_c^{-1} , however, disappears for lapse time greater than 30 sec in the same frequency range as well as for higher frequencies 6 and 12 Hz for lapse time greater than 20 sec.

We interpret the above observation as follows: since quarry blasts are shot at extremely shallow depth (35 feet), they generate more surface waves than earthquakes. These surface waves attenuate quickly because their propagation path is confined to shallow depths where seismic attenuation is strong. Body waves thus become dominant over surface waves for $t > 20$ sec at 6 and 12 Hz and for $t > 30$ sec at 1.5 and 3.0 Hz. Once body waves dominate over surface waves, the coda decay rate becomes the same for quarry blasts and earthquakes.

The above observed coda decay rate between quarry blasts and earthquakes leads us to our basic idea for discrimination, namely, the comparison of their power spectra $P_o(\omega)$ inferred at a time later than t_f at a single station. These power spectra $P_o(\omega)$ will not be influenced by surface waves and will not depend on media properties, since body waves dominate the late coda waves of both quarry blasts and earthquakes, with the same scattering and attenuation properties. We have chosen stations SIL and SDW for our power spectra comparison, because these two stations were operated satisfactorily through the time period from which our data were collected and were located close to both the quarry blasts and earthquakes used in this study (see Figure 1). Figure 3 shows

the coda power spectrum $P_o(\omega)$ vs. frequency for station SIL for earthquakes and quarry blasts, respectively. Each curve in these plots represents one event. We only plot those curves for which $P_o(\omega)$ is available for at least three frequency bands. All curves were normalized to the same value at frequency 1.5 Hz for convenience of comparison. In order to test the assumption of constant Q_c^{-1} for $t \geq t_r$, we also used a different reference time t_r with $t_r=20, 32, 40, 52$ sec corresponding to Figures 3a, 3b, 3c, and 3d for earthquakes and Figures 3e, 3f, 3g, and 3h for quarry blasts. We can see that $P_o(\omega)$ in Figure 3b is very similar to those in figures 3c and 3d. The same feature is also observed in figures 3f, 3g, and 3h for quarry blasts. The shape of the power spectrum $P_o(\omega)$ is not affected very much by the choice of t_r as long as $t_r > 30$ sec, which confirms the validity of our assumption that Q_c^{-1} is constant for $t \geq t_r$. By comparing earthquake power spectrum $P_o(\omega)$ with that of quarry blasts at the same reference time t_r (such as Figures 3a and 3e, 3b and 3f, etc.), we see that there is a significant difference between these two groups. The power spectra $P_o(\omega)$ of quarry blasts are decreasing more quickly than earthquakes with increasing frequency, indicating that the quarry blast source generates less high frequency energy than earthquakes. The same comparison was also made between earthquakes and quarry blasts at station SDW. The results are consistent with those from station SIL. This difference in source spectra frequency dependence, therefore, can be used for seismic discrimination between quarry blasts and earthquakes.

To check the depth and magnitude effects on the power spectrum of earthquakes and quarry blasts, we also chose one of the shallower earthquakes (focal depth of 0.6 km), one of the deeper earthquakes (focal depth of 11.9 km), and one of the quarry blasts for comparison. The magnitude of these three events are nearly the same (2.4 ~ 2.5). The seismograms of the quarry blast, the shallow earthquake and the deeper one for station SIL are shown in Figures 4a, 4b and 4c. The top traces in these figures show the unfiltered seismograms while the other traces show the results of band pass filtering of the seismograms with center frequencies of 1.5, 3, 6, and 12 Hz. The maximum amplitude of these three events are almost the same from a comparison of their unfiltered seismograms. However, for the band pass seismograms at 12 Hz, the quarry blast amplitude is significantly smaller when compared to the two earthquakes.

The time dependent spectral characteristics of these three events are plotted in Figures 5a, 5b and 5c. The contour lines in these figures show the iso-amplitude spectrum line plotted in the frequency-time diagram. The frequency range is 1 to 25 Hz,

and the lapse time range is from 0 to 50 sec. The frequency-time dependence of the amplitude spectra contour is distinctly different between the earthquakes and the quarry blast. The spectra for the quarry blast shows very rapid decay with increasing frequency while those for earthquakes cover much broader spectral ranges. Figure 6 shows the power spectrum $P_o(\omega)$ vs. frequency for the deep earthquake (line 1), the shallow one (line 2) and the quarry blast (line 3). The depth difference between the quarry blast and the shallow earthquake is about a half km while the difference between the shallow earthquake and the deep one is about 11 km. Thus, we can conclude that the depth effect is not the main reason for causing the source spectrum shape difference between quarry blasts and earthquakes in our results.

Therefore, we can conclude that the observed source spectrum difference between earthquakes and quarry blasts are mainly due to different source processes, such as the difference in source mechanism and the interaction between source and near-source media. This is physically reasonable because the quarry blasts are shot at shallow depths and the near-source media are less consolidated than the media generating earthquakes, which may result in a lack of high frequency energy generated compared to the earthquakes.

3. SEISMIC SCATTERING THEORY FOR SURFACE WAVES AND BODY WAVES AND ITS IMPLICATION OF DISCRIMINATION TO EXPLOSION-EARTHQUAKE AT REGIONAL DISTANCE

In the preceding section, we have shown that at local distances, if we can properly remove the path effects from the observed power spectra, we can discriminate the quarry blast and the earthquake from the shape of the source power spectra. For local events, coda Q_c^{-1} method provides an effective mean to isolate the source effect from path effects as shown above. To extend this discrimination method to the discrimination of explosions and earthquakes at regional distances, we need a proper means to remove the path effects at regional distances. Since shallow events produce significant surface waves, a complete scattering theory must include the scattering processes of surface waves, and the coupling process between body waves and surface waves. In this section, we shall develop an energy transfer theory for a mixture of surface wave and body wave to study their scattering and coupling processes. Using this theory we shall, first, explain the physical basis for successful discrimination of quarry blasts and earthquakes at local distances described in the preceding chapter. Then, by fitting our synthetic coda

attenuation curves with the observed data, we will estimate the scattering and coupling coefficients. Finally, with the derived scattering and coupling coefficients, we shall simulate the surface wave and body waves scattering processes at regional distances and investigate the feasibility of discrimination of explosions and earthquakes at regional distance by using the coda Q_c^{-1} method.

3.1 Energy transfer theory for Rayleigh wave

In this section, we shall consider a simple case in which the background medium is a homogeneous half-space. The only surface wave in this case is the Rayleigh wave. For simplicity, we neglect the conversions between the body waves and the Rayleigh wave. Then the energy distribution of Rayleigh wave in an absorption and scattering medium at an arbitrary point \mathbf{x} for frequency ω can be written as,

$$E^R(\mathbf{x}, \omega) = G(\mathbf{x}, \mathbf{x}_s) \exp[-\eta^R |\mathbf{r} - \mathbf{r}_s|] \epsilon^R_s(\mathbf{x}_s, \omega) + \sum_j \sigma(\mathbf{x}_j) G(\mathbf{x}, \mathbf{x}_j) \exp[-\eta^R |\mathbf{r} - \mathbf{r}_j|] E^R(\mathbf{x}_j, \omega), \quad (8)$$

Where, $\mathbf{r} = \mathbf{x} - \hat{\mathbf{e}}_z(\mathbf{x} \cdot \hat{\mathbf{e}}_z)$ is a horizontal vector, and η^R is the attenuation coefficient that includes the intrinsic (η_i^R) and scattering attenuation (η_s^R), i.e., $\eta^R = \eta_i^R + \eta_s^R$. In eq.(8), $E^R(\mathbf{x}, \omega)$ is the seismic energy per unit volume carried by Rayleigh wave at point \mathbf{x} and frequency ω . The first term in the right-hand-side of (8) represents the direct Rayleigh wave energy radiated from source, and the second term in the right-hand-side of (8) describes the total scattering energy from all scatters (\mathbf{x}_j). Where σ is the scattering cross-section, $G(\mathbf{x}, \mathbf{x}_j)$ and $\exp[-\eta^R |\mathbf{r} - \mathbf{r}_j|]$ describes the geometrical spreading and attenuation, respectively. It should be noted that the attenuation is caused only by the horizontal propagation, since the surface wave only propagates horizontally. For weak scattering case, the scattering cross-section σ can be analytically derived by using Born approximation (Aki and Richards, 1980). Here, for simplicity, we assume that σ is a constant. The geometrical spreading function $G(\mathbf{x}, \mathbf{x}')$, however, can be determined by the consideration of energy conservation.

Geometrical Spreading Function of Rayleigh Wave:

The direct Rayleigh wave (Rayleigh wave in the background medium) has the following form (Aki and Richards, 1980),

$$U^R(x, \omega) = \frac{\mathbf{P}_R(x)[\mathbf{P}_R(x_s) \cdot \mathbf{F}(x_s)]}{\sqrt{(\pi/2)k_R|\mathbf{r}-\mathbf{r}_s|}} \exp\{i[k_R|\mathbf{r}-\mathbf{r}_s| + \pi/4]\}, \quad (9)$$

where,

$$\mathbf{P}_R(x) = r_1(z, \omega)\hat{\mathbf{e}}_r + ir_2(z, \omega)\hat{\mathbf{e}}_z, \quad (9a)$$

with $\hat{\mathbf{e}}_r = (\mathbf{r}-\mathbf{r}_s)/|\mathbf{r}-\mathbf{r}_s|$. The corresponding energy density is

$$E_o^R(x, \omega) = \frac{1}{2}\rho\omega^2|U^R(x, \omega)|^2 = \frac{\rho\omega^2}{\pi k_R} \frac{|\mathbf{P}_R(z)|^2}{|\mathbf{r}-\mathbf{r}_s|} |\mathbf{P}_R(x_s) \cdot \mathbf{F}(x_s)|^2. \quad (10)$$

For steady state, the energy rate should be a constant for any closed-surface that encloses the source, namely,

$$\oint_S \{E_o^R(x, \omega)v_R\} \cdot \hat{\mathbf{s}} dS = \text{constant}, \quad \text{for } x_s \text{ inside } S. \quad (11)$$

Where, $\hat{\mathbf{s}}$ is the normal vector of the surface element dS , and v_R is the velocity vector of the Rayleigh wave. Since the surface wave propagates along the horizontal direction, we consider a cylindrical surface that leads to a simple surface integration,

$$\oint_S \{E_o^R(x, \omega)v_R\} \cdot \hat{\mathbf{s}} dS = \int_0^{+\infty} dz \int_0^{2\pi} R d\theta E_o^R(x, \omega)v_R.$$

Where, $R = |\mathbf{r}-\mathbf{r}_s|$. Substituting eq.(10) in (11), we find

$$\begin{aligned} \varepsilon_o^R(x_s) &= \frac{1}{v_R} \oint_S \{E_o^R(x, \omega)v_R\} \cdot \hat{\mathbf{s}} dS = \frac{2\omega^2\rho}{k_R} \int_0^{+\infty} |\mathbf{P}_R(z)|^2 dz |\mathbf{P}_R(x_s) \cdot \mathbf{F}(x_s)|^2 \\ &= \frac{2\rho\omega^2}{k_R} |\mathbf{F}(x_s)|^2 \{ |r_1(z_s)n_r|^2 + |r_2(z_s)n_z|^2 \} \int_0^{+\infty} \{ |r_1(z)|^2 + |r_2(z)|^2 \} dz. \end{aligned} \quad (12)$$

Using the above result, eq. (10) can be rewritten as

$$E_o^R(\mathbf{x}, \omega) = \frac{g_R(z, \omega)}{2\pi|\mathbf{r}-\mathbf{r}_s|} \epsilon_o^R(\mathbf{x}_s), \quad (13)$$

where,

$$g_R(z, \omega) = \frac{|\mathbf{P}_R(z)|^2}{\int_0^{+\infty} |\mathbf{P}_R(z')|^2 dz'} = \frac{[r_1(z, \omega)^2 + r_2(z, \omega)^2]}{\int_0^{+\infty} [r_1(z', \omega)^2 + r_2(z', \omega)^2] dz'} . \quad (13a)$$

Thus, we obtain the geometrical spreading function of Rayleigh wave energy propagation as

$$G(\mathbf{x}, \mathbf{x}') = \frac{g_R(z, \omega)}{2\pi|\mathbf{r}-\mathbf{r}'|} . \quad (14)$$

From equation(6a), we can verify the following identity,

$$\int_0^{+\infty} g_R(z, \omega) dz = 1 . \quad (14a)$$

Integral equation of scattering Rayleigh wave in random medium:

We are now ready to set up the basic integral equation for Rayleigh wave scattering in random medium. Substituting eq.(14) in (8), and assuming that the random scatters are uniformly distributed and can be described by a continuous distribution n_o (density of scatters), we obtain the following integral equation,

$$E^R(\mathbf{x}, \omega) = \frac{g_R(z, \omega) e^{-\eta^R |\mathbf{r}-\mathbf{r}_s|}}{2\pi|\mathbf{r}-\mathbf{r}_s|} \epsilon_o^R(\mathbf{x}, \omega) + \int_V \eta_s^R \frac{g_R(z, \omega)}{2\pi|\mathbf{r}-\mathbf{r}'|} e^{-\eta^R |\mathbf{r}-\mathbf{r}'|} E^R(\mathbf{x}, \omega) dV(\mathbf{x}') , \quad (15)$$

where, $\eta_s^R = n_o \sigma$. Eq.(15) is similar to the energy transfer equation for body wave (Wu, 1985; Zeng et al., 1991), but with different geometrical spreading functions and the attenuation factors that are caused by the characterizations of surface wave propagation. The dependence of $|\mathbf{r}-\mathbf{r}'|$ indicates the horizontal propagation property of the surface

wave, whereas, the $g_R(z, \omega)$ explores the depth distribution of surface wave energy. Integral equation (15) can be solved by using spatial domain Fourier transform method. First, we note that equation (15) can be rewritten as

$$E^R(x, \omega) = g_R(z, \omega) E_2^R(r, \omega). \quad (16)$$

Inserting equation (16) into (15) and using the identity (14a), we obtain

$$E_2^R(r, \omega) = \frac{e^{-\eta^R |r-r_s|}}{2\pi |r-r_s|} \epsilon_o^R(x_s, \omega) + \int_{\Sigma} \eta_s^R \frac{e^{-\eta^R |r-r'|}}{2\pi |r-r'|} E_2^R(r', \omega) d\Sigma(r'). \quad (17)$$

Here, $\Sigma(r) = \{(x, y) | -\infty < x < +\infty, -\infty < y < +\infty\}$. The corresponding Fourier transform is

$$\tilde{E}_2^R(k, \omega) = \tilde{G}_2^R(k) \epsilon_o^R(x_s, \omega) + \eta_s^R \tilde{G}_2^R(k) \tilde{E}_2^R(k, \omega). \quad (18)$$

Where, we assumed $r_s = 0$, and $\tilde{G}_2^R(k, \omega)$ is given by

$$\tilde{G}_2^R(k, \omega) = \iint_{-\infty}^{+\infty} dx dy \frac{e^{-\eta^R r}}{2\pi r} \exp(ik \cdot r) = \int_0^{+\infty} J_0(kr) e^{-\eta^R r} dr = \frac{1}{\sqrt{k^2 + (\eta^R)^2}}. \quad (18a)$$

Substituting this result in eq.(18), then taking the inverse Fourier transform over k , we finally obtain

$$E^R(x, \omega) = g_R(z, \omega) P_R(r, \eta^R, \eta_s^R) \epsilon_o^R(x_s, \omega), \quad (19)$$

where $P_R(r, \eta^R, \eta_s^R)$ is the inverse Fourier transform of $\tilde{G}_2^R(k, \omega)$,

$$P_R(r, \eta^R, \eta_s^R) = \frac{1}{2\pi} \int_0^{+\infty} J_0(kr) \frac{k dk}{\sqrt{k^2 + (\eta^R)^2} - \eta_s^R}. \quad (19a)$$

Solution (19) has a clear physical meaning. The term $\epsilon_o^R(x_s, \omega)$, as defined earlier, contains the seismic source information. Function $g_R(z, \omega)$ represents the depth dependence of Rayleigh wave energy, whereas the function $P_R(r, \eta^R, \eta_s^R)$ describes the propagation and attenuation processes of the Rayleigh wave energy. $P_R(r, \eta^R, \eta_s^R)$ can be obtained by evaluating integral (19a). For a pure absorption medium ($\eta_s^R = 0$), we find

$P_R(r, \eta^R, 0) = e^{-\eta^R r} / 2\pi r$. This is consistent with our direct Rayleigh wave (solution in background medium). For general absorption and scattering media, we can numerically evaluate the propagation and attenuation function $P_R(r, \eta_i^R, \eta_s^R)$.

It is noted that equation (15) describes a stationary energy transfer process, i.e., $E^R(x, \omega)$ represents the amplitude of the spectrum of scattered Rayleigh wave. To obtain the time-history of the scattered Rayleigh energy for a given frequency ω and the observational point x , we introduce a time-delay phase factor of $\exp[-i\Omega|r - r'|/c_R]$, then take inverse Fourier transform over frequency Ω . During the inverse Fourier transformation, the frequency ω is kept as a constant which is defined as center frequency. Thus we can obtain the time-history of scattered energy for a given frequency ω . Figure 7 shows the energy distributions for the case of $\eta_i^R = 0.01 \text{ km}^{-1}$, $\eta_s^R = 0.02 \text{ km}^{-1}$ and $\omega = 1 \text{ Hz}$. As we expected the scattered energy arrived at time of $t = |r - r'|/c_R$.

3.2 Energy transfer theory for S and Rayleigh waves' scattering processes

In the preceding section, we have considered only the scattering processes of surface waves, and neglected the body waves' conversions. In this section, we shall consider the coupling effect of body waves with surface waves. For simplicity, we consider only the coupling process between the S wave and Rayleigh wave. The energy transfer equation described such an coupled scattering process can be written as follows,

$$E^R(x, \omega) = G^R(x, x_s) \cdot e^{-\eta^R |r - r_s|} \epsilon_o^R(x_s, \omega) + \int_V G^R(x, x') \cdot e^{-\eta^R |r - r'|} \{ \eta_s^{RR} E^R(x', \omega) + \eta_s^{SR} E^S(x', \omega) \} dV(x'), \quad (20a)$$

$$E^S(x, \omega) = G^S(x, x_s) \cdot e^{-\eta^S |r - r_s|} \epsilon_o^S(x_s, \omega) + \int_V G^S(x, x') \cdot e^{-\eta^S |r - r'|} \{ \eta_s^{RS} E^R(x', \omega) + \eta_s^{SS} E^S(x', \omega) \} dV(x'), \quad (20b)$$

where,

$E^S(x, \omega)$: seismic energy carried by S wave per unit volume at x ;

$E^R(x, \omega)$: seismic energy carried by Rayleigh wave per unit volume at x ;

η^R : total attenuation coefficient for Rayleigh wave, $\eta^R = \eta_i^R + \eta_s^{RR} + \eta_s^{SR}$;

η_s^{RR} : Rayleigh to Rayleigh waves scattering coefficient;

η_s^{SR} : S to Rayleigh waves scattering coefficient;

η^S : total attenuation coefficient for S wave, $\eta^S = \eta_i^S + \eta_s^{RS} + \eta_s^{SS}$;

η_i^S : absorption coefficient for S wave;

η_s^{RS} : Rayleigh to S waves scattering coefficient;

η_s^{SS} : S to S waves scattering coefficient;

$\epsilon_0^S(\mathbf{x}_s, \omega)$: rate of S wave energy rate radiated from source divided by the velocity of S wave;

$\epsilon_o^R(\mathbf{x}_s, \omega)$: rate of Rayleigh wave energy radiated from source divided by velocity of Rayleigh wave;

$G^S(\mathbf{x}, \mathbf{x}')$: the geometrical spreading function for S wave in a half-space medium, and it can be approximated by

$$G^S(\mathbf{x}, \mathbf{x}') = \frac{1}{4\pi|\mathbf{x}-\mathbf{x}'|} + \frac{1}{4\pi|\mathbf{x}-(\mathbf{x}')^*|},$$

where, $(\mathbf{x}')^*$ is the image point of \mathbf{x}' with respect to the free surface $z=0$, i.e., $(\mathbf{x}')^*=(x', y', -z')$.

Equations (20a) and (20b) can be further simplified. Making a two-dimensional Fourier transform over the horizontal variable (x, y) , equation (20a, b) can be reduced to,

$$\tilde{E}^R(K, z, \omega) = \tilde{G}^R(K, z; z_s; \omega) \epsilon_o^R(\mathbf{x}_s, \omega) \quad (21a)$$

$$+ \int_0^{+\infty} \tilde{G}^R(K, z; z'; \omega) \{ \eta_s^{RR} \tilde{E}^R(K, z', \omega) + \eta_s^{SR} \tilde{E}^S(K, z', \omega) \} dz',$$

$$\tilde{E}^S(K, z, \omega) = \tilde{G}^S(K, z; z_s; \omega) \epsilon_o^S(\mathbf{x}_s, \omega) \quad (21b)$$

$$+ \int_0^{+\infty} \tilde{G}^S(K, z; z'; \omega) \{ \eta_s^{RS} \tilde{E}^R(K, z; z'; \omega) + \eta_s^{SS} \tilde{E}^S(K, z; z', \omega) \} dz',$$

where, K is the horizontal wave-number and

$$\tilde{G}^S(K, z; z'; \omega) = \int_0^{+\infty} G(r, z; z'; \omega) \exp(-\eta^s \sqrt{r^2 + (z-z')^2}) J_0(Kr) r dr,$$

and

$$\tilde{G}^R(K, z; \omega) = g(z, \omega) \int_0^{+\infty} \exp(-\eta^R r) J_0(Kr) dr .$$

Solving the coupled equations (21a) and (21b), we can obtain the solution of energy transfer processes of S and Rayleigh waves. The time-history of total scattering energy can be determined by introducing proper time-delay phase factors to these coupled equations. Figure. (8) show the time history of total scattering energy of S and Rayleigh waves, for the case of $\eta_i^S=0.01(\text{km})^{-1}$, $\eta_s^{RS}=0.01(\text{km})^{-1}$, $\eta_s^{SS}=0.02(\text{km})^{-1}$, $\eta_i^R=0.03(\text{km})^{-1}$, $\eta_s^{RR}=0.02(\text{km})^{-1}$ and $\eta_s^{SR}=0.01(\text{km})^{-1}$ for various source depths. Our results indicate that the shallower the source depth locates or the lower the frequency is, the contribution of scattering Rayleigh waves is larger. This is consistent with the observed results of Su and Aki (1991) as shown in Figure 2, where earthquakes have an averaged focal depth of 8 km, whereas the averaged focal depth of quarry blasts is about 10m.

To quantitatively interpret the observation shown in Figure 2, and determine the coupling coefficients, we shall compare our synthetic attenuation curves with the observed ones. The synthetic attenuation curves are calculated using the same method as described in section 2.1 from our theoretical scattered S wave energy envelope. We here consider only the S wave coda attenuation, Q_c^{-1} , that mainly includes the S to S waves scattering as well as Rayleigh to S waves scattering. For simplicity, we neglect the S to Rayleigh conversions, thus the only coupling coefficient needs to be determined is η_s^{RS} . Physically, the discrimination between the earthquakes and quarry blasts can be attributed to the contributions of Rayleigh wave, namely, the measure of coda attenuation of quarry blasts contains significant Rayleigh wave's conversions because of the shallow focal depth, while the coda attenuation of the earthquakes contains little Rayleigh waves conversions because of the deeper focal depth. Based on this point we shall, first, determine the S wave's intrinsic and scattering coefficients, i.e., η_i^S and η_s^{SS} , by matching our synthetic S wave's attenuation with the observed earthquake's coda attenuation, Q_c^{-1} . At this stage we let $\eta_s^{RS}=0$. Having the coefficients of η_i^S and η_s^{SS} , we then determine the coefficients of η_s^{RS} , η_s^{RR} and η_i^R by fitting our synthetic attenuation curves with the observed quarry blasts coda attenuation, Q_c^{-1} .

After more than 20 trials, we found the attenuation coefficients for the best matching with the observed data as given in Table 1. And the corresponding coda attenuation curves are shown in Figure 9. Our results indicate that the coupled scattering

coefficients, η_s^{rs} , which describes the scattering conversion from Rayleigh wave to S wave, are strongly depends on frequency in the following way: for frequency lower than 3 Hz, $\eta_s^{rs}=0.05 \text{ km}^{-1}$; while for frequency greater than 6 Hz $\eta_s^{rs}<0.0005 \text{ km}^{-1}$. Therefore, there may exist a critical frequency between 3 Hz and 6 Hz beyond which the Rayleigh wave conversions are negligible, while below which the Rayleigh wave conversions to S wave are significant.

3.3 Discussion on the Discrimination of Earthquakes and Explosions at Regional Distance

Having the theoretical studies on the discrimination of earthquakes and quarry blasts at local distance, we can discuss the possibility of the discrimination of earthquakes and explosions at regional distance using the coda method. In the following discussion we assume that the intrinsic and scattering attenuation coefficients of S and Rayleigh waves, and the coupled scattering coefficients obtained in the above study are still valid for the events at regional distance. Using those derived coefficients we calculated the synthetic coda attenuation curves for earthquakes and explosions at regional distances as shown in Figure 10. Here, we assume that the hypocenter is 600 km, and the focal depth is 10 km for earthquakes and 0.01 km for explosions. As shown in Figure 10, our theoretical simulations show that the Rayleigh wave conversion to scattered S wave at regional distance is much more significant than that at local distance, because the Rayleigh wave has a weaker geometrical spreading factor than S wave. For lower frequency (e.g., f=3 Hz or 1.5Hz), the synthetic result predicts a strong increase in coda attenuation that starts just after the Rayleigh wave's arrival and last about 50 seconds. For higher frequency (e.g., f=6 Hz or 12 Hz), a similar increase is also predicted by our synthetic result, although it is not as strong as the one for lower frequencies. It should be pointed out that this increase in the coda attenuation estimate for lower frequency is an upper-bound, the actual predicted increase in coda attenuation should be below this amount; because the value of coupled scattering coefficient η_s^{rs} is given in the range of 0 to 0.0005 km^{-1} .

In order to compare the above result with the observation, we have analyzed the regional events recorded by the Chinese Digital Seismic Network (CDSN). Figure 11 shows the seismograms of the earthquakes and explosions used in this analysis. These seismograms are recorded by the CDSN at AKK station. The results of our analysis, i.e., the coda Q_c^{-1} of S-wave for both the explosions and earthquakes are plotted in Figure 12,

which show a similar result as predicted only for the high frequency case. The reason why our theoretical predictions fail for the low frequency case is due to the absence of the crustal layer in our model. When frequency becomes low, the corresponding wavelength becomes comparable to the thickness of the crust, therefore, the crustal effects on the seismic scattering cannot be neglected. In the future study, we shall consider the crustal effects on the seismic waves scattering processes, in order to obtain a more complete scattering theory at regional distances.

4. DISCUSSIONS AND CONCLUSIONS

We have successfully discriminated the quarry blasts and earthquakes at local distance from the observed source power spectra by using the coda Q method. To extend this discrimination method to the events at regional distances, we have developed the energy transfer theory for a mixture of Rayleigh and S wave's propagation in a random scattering and attenuation medium. Applying this theory to the quarry blast-earthquake problem at local distance, we can explain the observations satisfactorily. Our study indicates that the Rayleigh waves' scattering become important for the events with shallower focal depth such as the quarry blasts and nuclear explosions. By fitting our theoretical attenuation curves to the observed ones at local distances, we have obtained the S and Rayleigh waves' intrinsic and scattering coefficients, and the coupled scattering coefficient of Rayleigh with S waves. Assuming that these coefficients are valid for the events at regional distances, we have compared the predicted and observed coda envelope at regional distances for the purpose of discrimination between the earthquakes and explosions at regional distance. Our prediction shows that the Rayleigh wave's contributions become more significant for shallower events (explosions), while for deeper events (earthquakes) the Rayleigh wave's contributions are still negligible. Comparison between predicted and the data of CDSN suggests that the discrimination of earthquakes and explosions at regional distance may be possible by using the coda method for the high frequency case. For the low frequency case, we must consider the crustal effects. In other words, a scattering theory for Lg waves is needed. We plan to do this work in the future.

REFERENCES

Aki, K. (1969). Analysis of seismic coda of local earthquakes as scattered waves, *J. Geophys. Res.*, **74**, 615-631.

Aki, K. and B. Chouet (1975). Origin of coda waves: source, attenuation and scattering effects, *J. Geophys. Res.*, **80**, 3322-3342.

Aki, K. and P. G. Richards (1980). *Quantitative Seismology: Theory and Methods*, W. H. Freeman, San Francisco.

Bennett, T. J. and J. R. Murphy (1986). Analysis of seismic discrimination capabilities using regional data from western United States events, *Bull. Seism. Soc. Am.*, **76**, 1069-1086.

Bennett, T. J., B. W. Barker, K. L. McLaughlin and J. R. Murphy (1989). Regional discrimination of quarry blasts, earthquakes and underground nuclear explosions, Report No. GL-TR-89-0114, Geophysics Laboratory, AFSC, Hanscom Air Force Base, MA 01731-5000.

Murphy, J. R. and T. J. Bennett (1982). A discrimination analysis of short-period regional seismic data recorded at Tonto Forest Observatory, *Bull. Seism. Soc. Am.*, **72**, 1351-1366.

Pomeroy, P. W., W. J. Best, and T. V. McEvilly (1982). Test ban treaty verification with regional data -- A review, *Bull. Seism. Soc. Am.*, **72**, S8-S129.

Smith, A. T. (1989). High-frequency seismic observations and models of chemical explosions: implications for the discrimination of ripple-fired mining blasts, *Bull. Seism. Soc. Am.*, **79**, 1089-1110.

Su, F., K. Aki, and N. N. Biswas (1991). Discriminating quarry blasts from earthquakes using coda waves, *Bull. Seism. Soc. Am.*, **81**, 161-178.

Wu, R. S. (1985). Multiple scattering and energy transfer of seismic waves--separation of scattering effect from intrinsic attenuation, I. Theoretical modeling, *Geophys. J. R. Astr. Soc.*, **82**, 57-80.

Zeng, Y. H., F. Su, and K. Aki (1991). Scattering wave energy propagation in a random isotropic scattering medium, I. Theory, *J. Geophys. Res.*, **96**, 607-620.

**Table 1. Inverted intrinsic, scattering
& coupling coefficients**

<i>frequency</i> (Hz)	η_i' (km ⁻¹)	η_s'' (km ⁻¹)	η_i'' (km ⁻¹)	η_s''' (km ⁻¹)	η_s'''' (km ⁻¹)
1.5	0.01	0.017	0.07	0.05	0.005
3.0	0.02	0.007	0.07	0.05	0.005
6.0	0.025	0.01	0.07	0.05	.00005
12.0	0.028	0.012	0.07	0.05	.00005

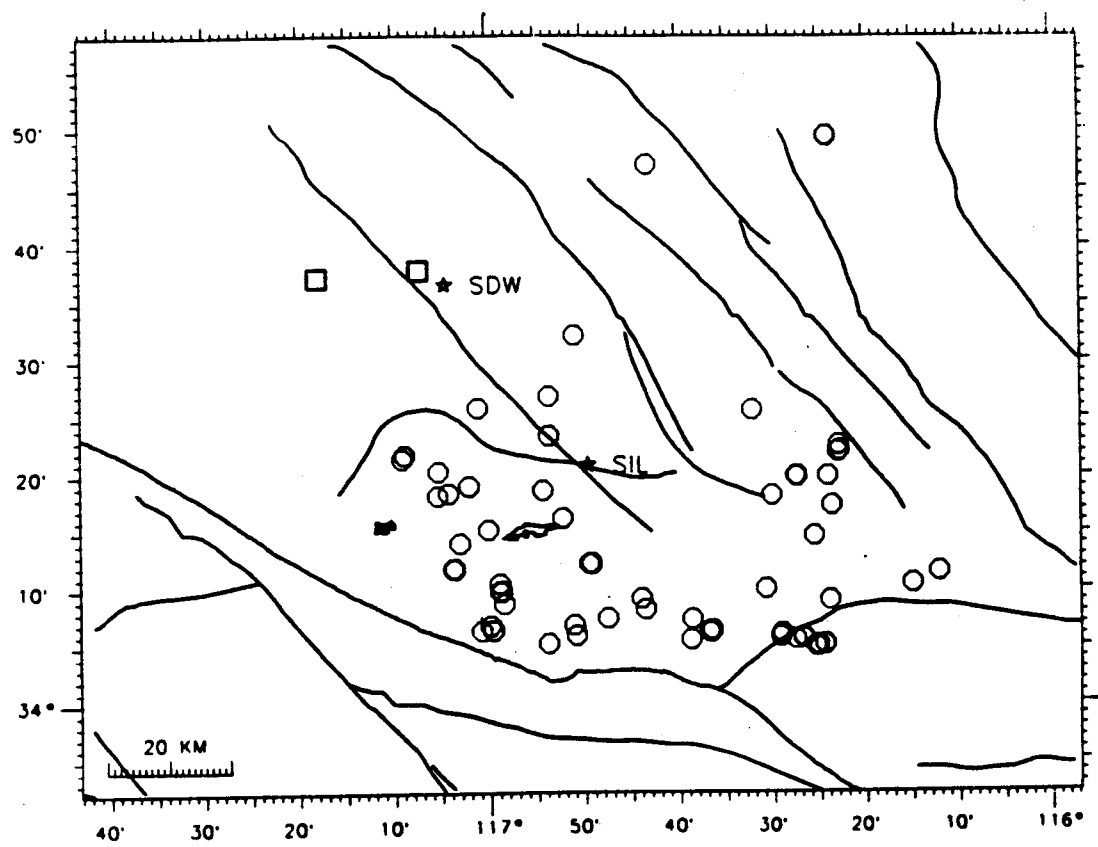


Figure 1. Map showing the epicenters of earthquakes (open circles) and quarry blasts (open squares) used in this study as well as the location of seismic stations (solid stars) and traces (solid lines). Note quarry blasts were shot repeatedly in two places.

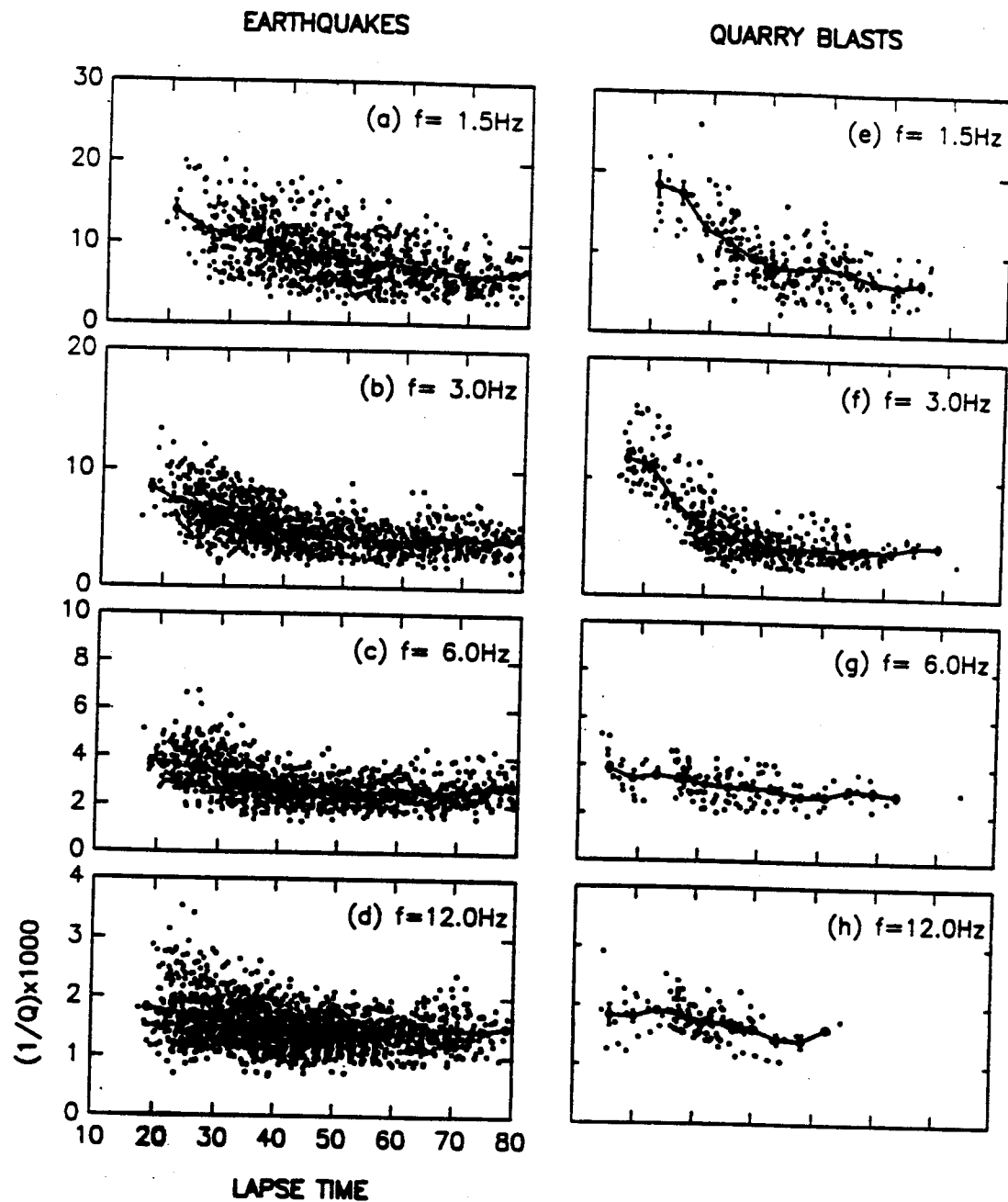


Figure 2: Coda Q_c^{-1} vs. lapse time obtained using the events shown in Figure 1 with (a), (b), (c), and (d) for earthquakes and (e), (f), (g), and (h) for quarry blasts. Each open circle on the plot represents one measurement for a particular seismogram on a time window of 34 sec for frequency 1.5 Hz, and 25 sec for 3 Hz, and 20 sec for 6 and 12 Hz. The solid line connects the mean points (solid circles) calculated by averaging the individual measurements in each 8 sec time interval with 4 sec overlapping at the adjacent mean points. The standard error of the mean is also shown for each mean point.

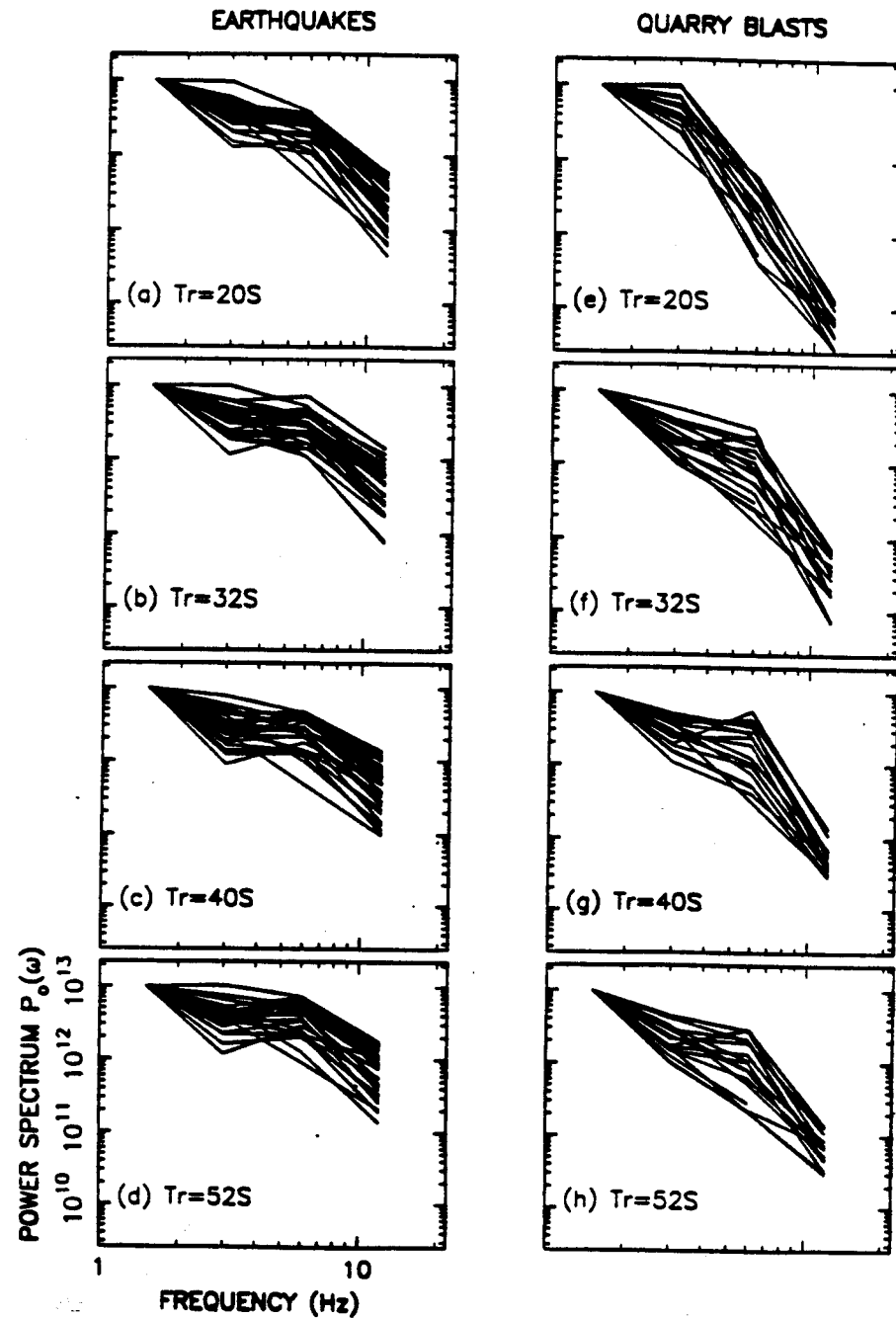


Figure 3: Power spectrum $P_o(\omega)$ vs. frequency obtained at station SIL with (a), (b), (c), and (d) correspond to reference times of 20, 32, 40, 52 sec for earthquakes and (e), (f), (g) and (h) for quarry blasts. Each curve on these plots represents one event. We only plotted those curves for which $P_o(\omega)$ is available for at least three frequency bands. All curves were normalized to the same values at frequency 1.5 Hz for convenience of comparison.

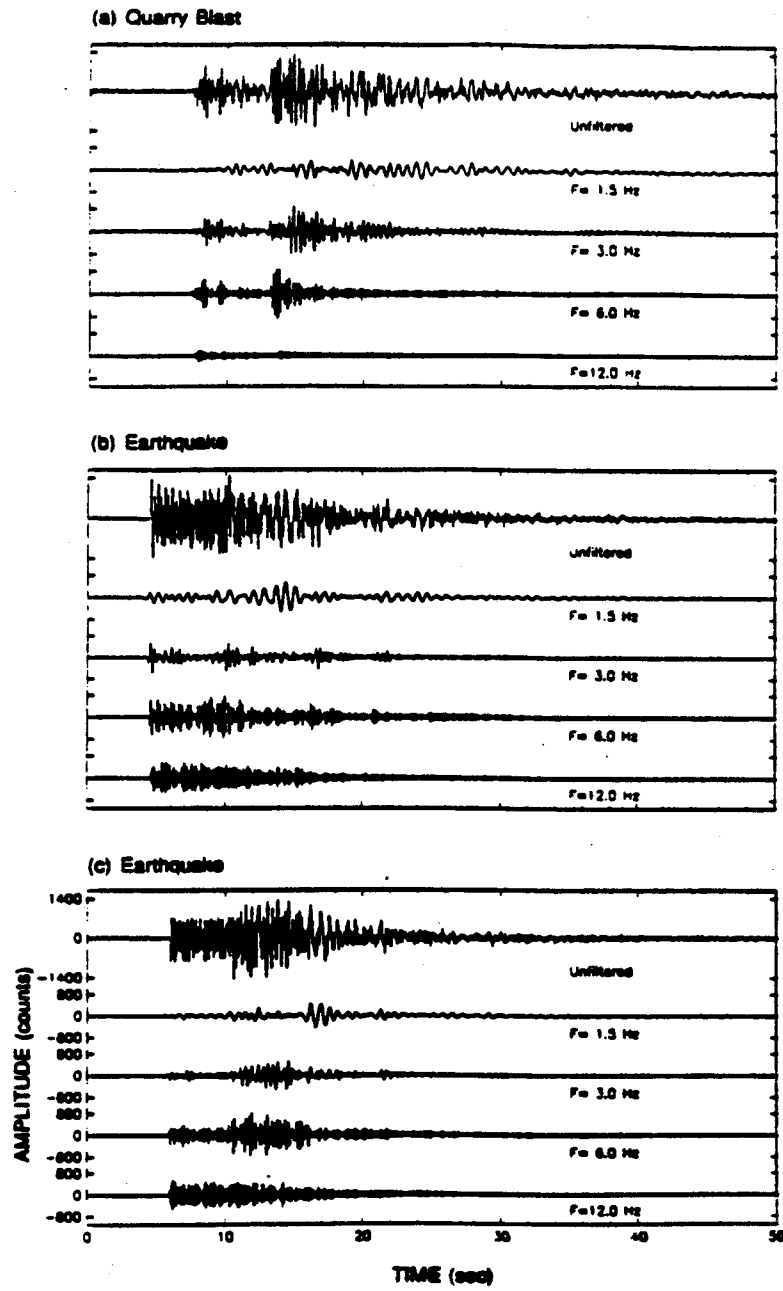


Figure 4: Seismograms of (a): a quarry blast (2/13/85, N34° 37.80', W117° 7.20', depth 0 km, magnitude 2.5, epicentral distance 41 km), (b): a shallow earthquake (5/6/86, N34° 20.31', W117° 5.28', depth 0.6 km, magnitude 2.4, epicentral distance 24 km), (c): a deep earthquake (5/31/86, N34° 6.43', W116° 36.58', depth 11.9 km, magnitude 2.4, epicentral distance 33 km), recorded at station SIL. The top unfiltered seismogram is followed by bandpass-filtered seismograms with center frequencies of 1.5, 3.6 and 12 Hz, respectively.

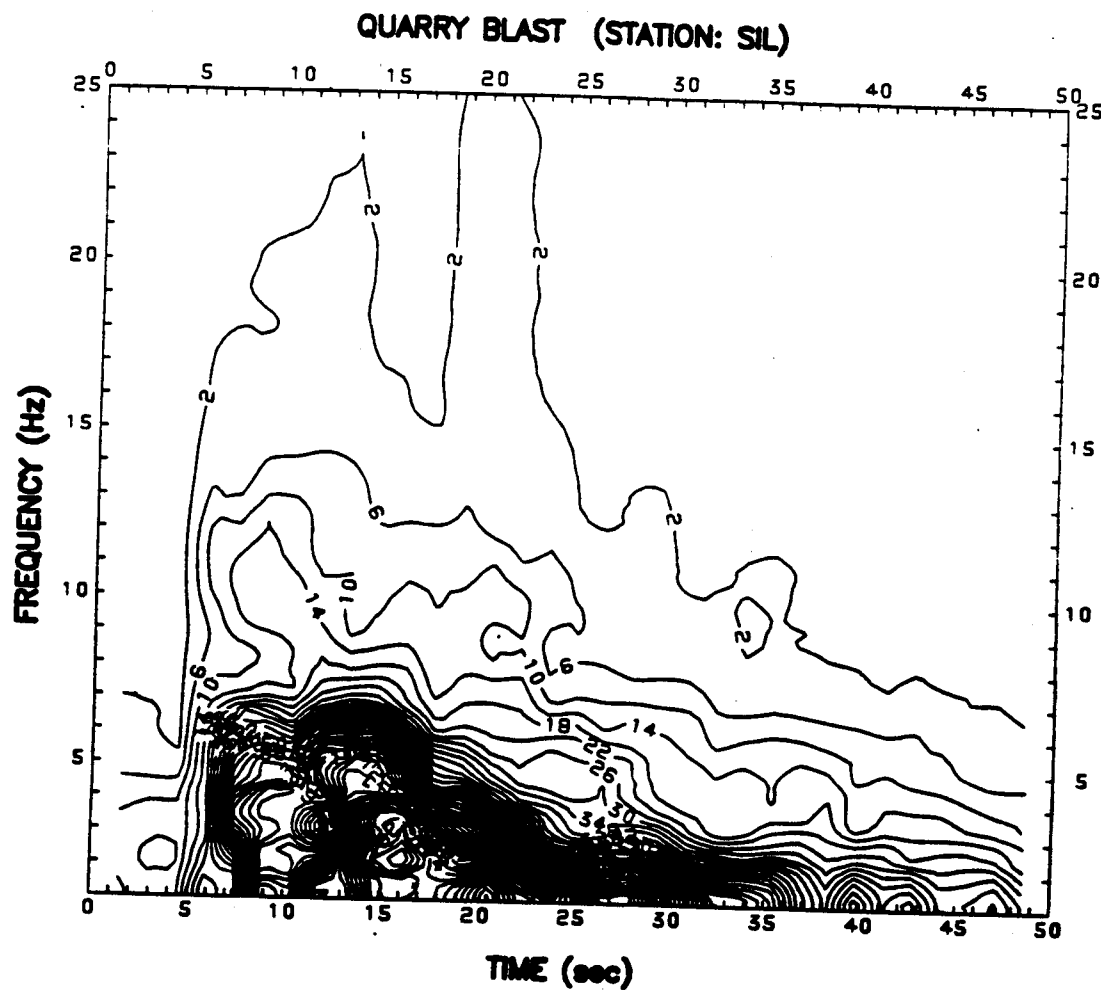


Figure 5a: Contours of amplitude spectra plotted in a frequency vs. time diagram for the quarry blast shown in Figure 4a.

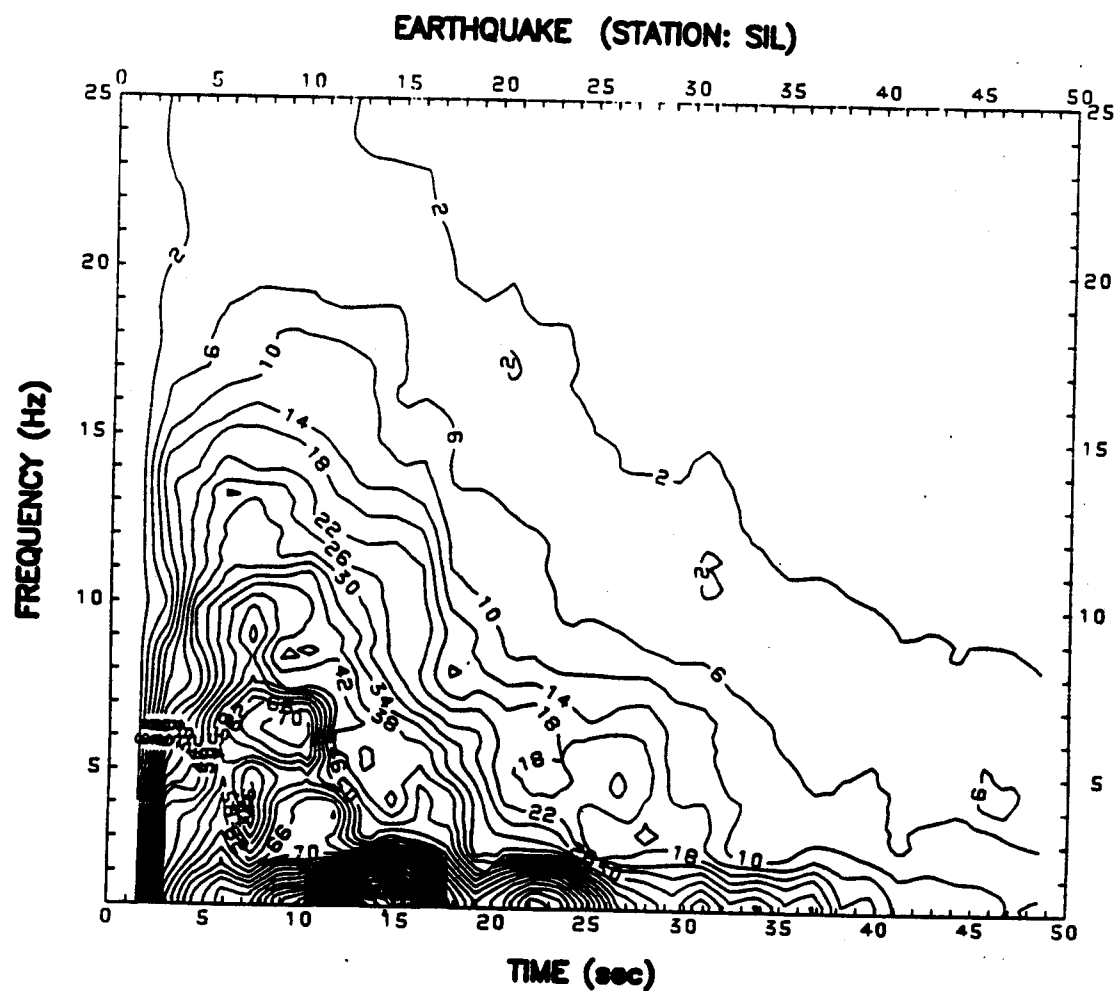


Figure 5b: Contours of amplitude spectra plotted in a frequency vs. time diagram for the shallow earthquake shown in Figure 4b.

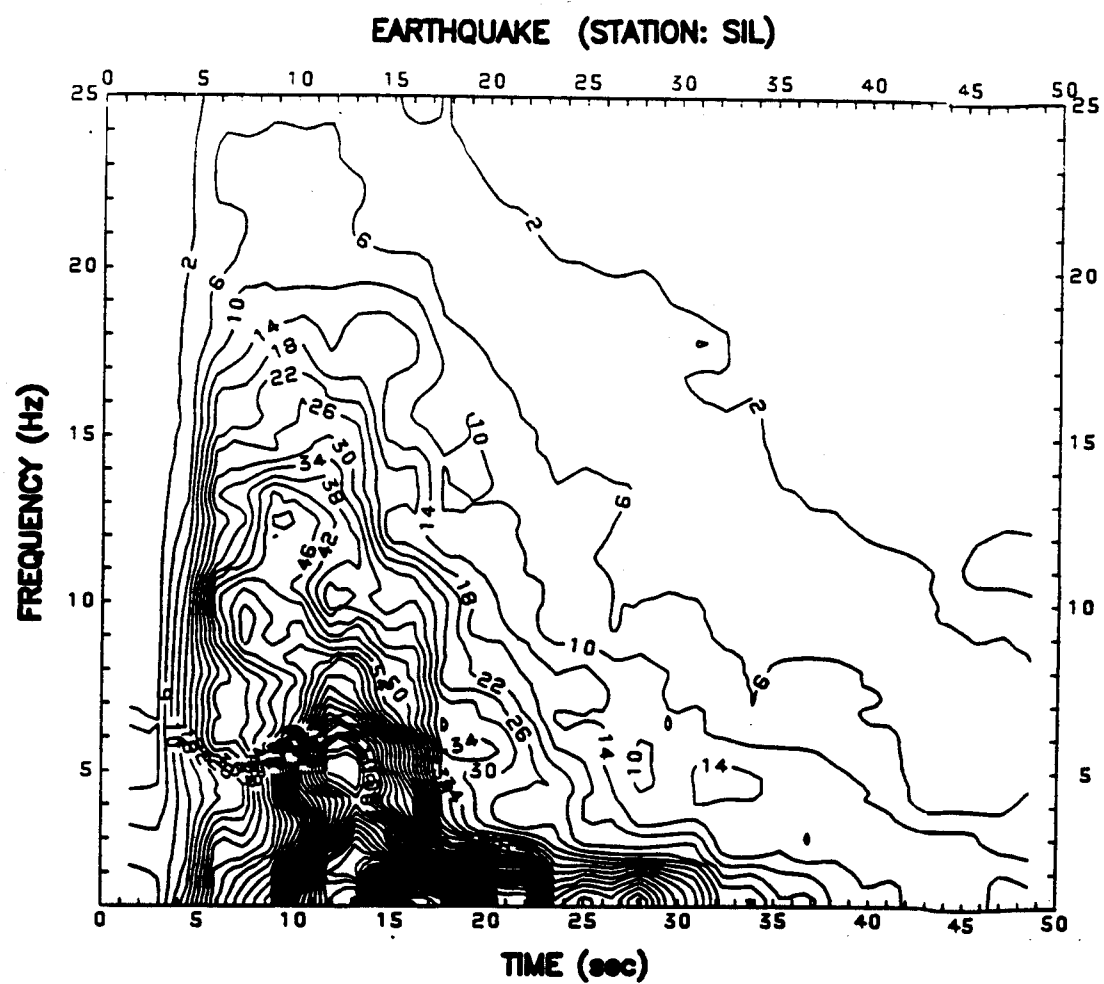


Figure 5c: Contours of amplitude spectra plotted in a frequency vs. time diagram for the deep earthquake shown in Figure 4c.

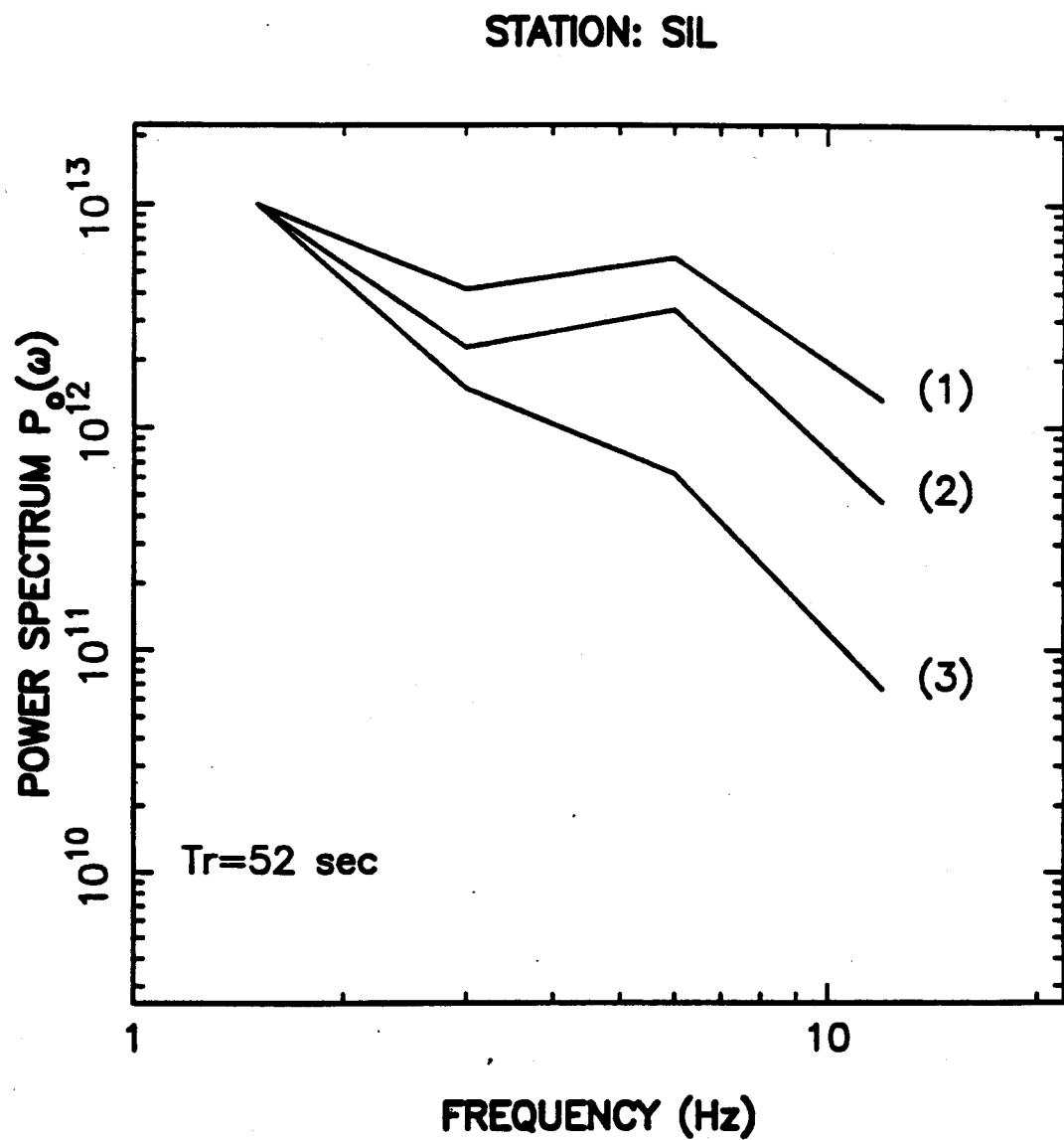


Figure 6: Power spectrum $P_o(\omega)$ vs. frequency for the deep earthquake (line 1), the shallow one (line 2), and the quarry blast (line 3), obtained at stations SIL at $t_r=52$ sec. The three curves were normalized to the same value at frequency 1.5 Hz for convenient of comparison.

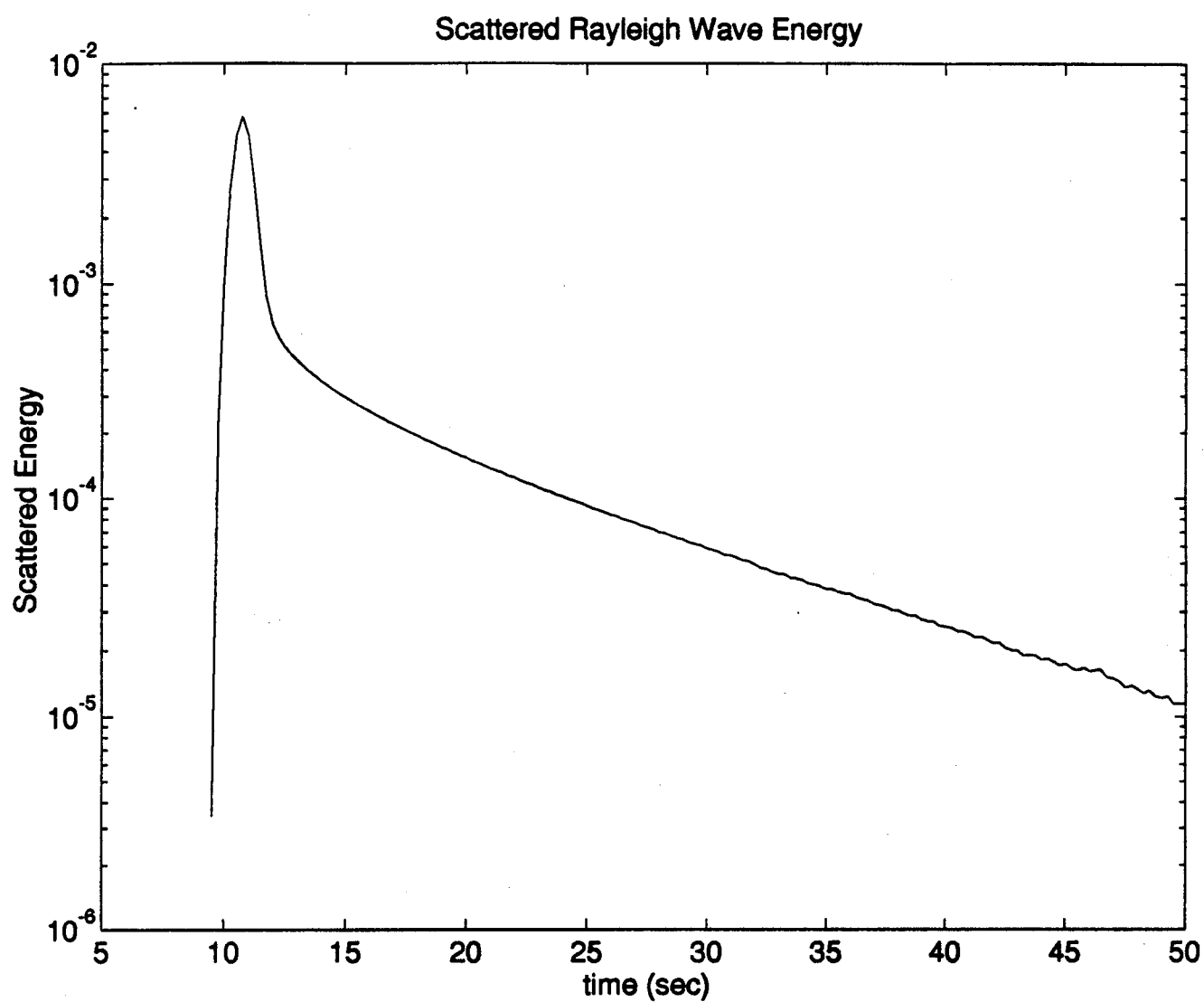


Figure 7: Seismic energy of scattered Rayleigh wave for the case of $\eta_i^R=0.03 \text{ (km)}^{-1}$, $\eta_s^R=0.02 \text{ (km)}^{-1}$ and $\omega=1\text{Hz}$. Where $r=30 \text{ km}$, and $c_R=2.8 \text{ km/sec}$.

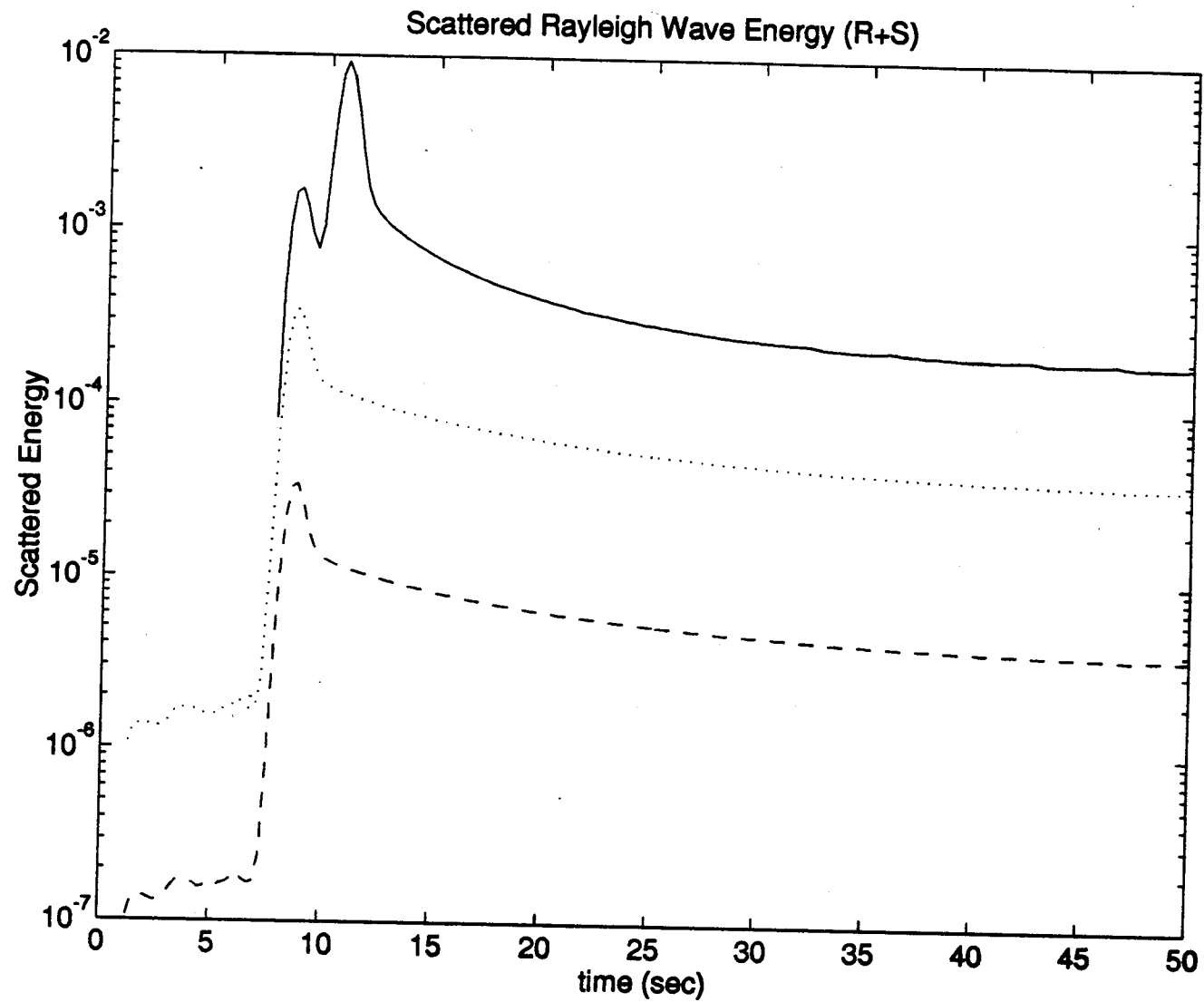


Figure 8: Focal depth and frequency ω dependence of total scattered energy of Rayleigh and S waves, where $\eta_i^R = 0.03 \text{ (km)}^{-1}$, $\eta_s^{RR} = 0.02 \text{ (km)}^{-1}$, $\eta_s^{SR} = 0.01 \text{ (km)}^{-1}$, $\eta_i^S = 0.01 \text{ (km)}^{-1}$, $\eta_s^{SS} = 0.02 \text{ (km)}^{-1}$, $\eta_s^{SS} = 0.01 \text{ (km)}^{-1}$ and $r = 30 \text{ km}$. For the cases of $z_s = 0.01 \text{ km}$ (solid line), $z_s = 1 \text{ km}$ (dotted line) and $z_s = 10 \text{ km}$ (dashed line).

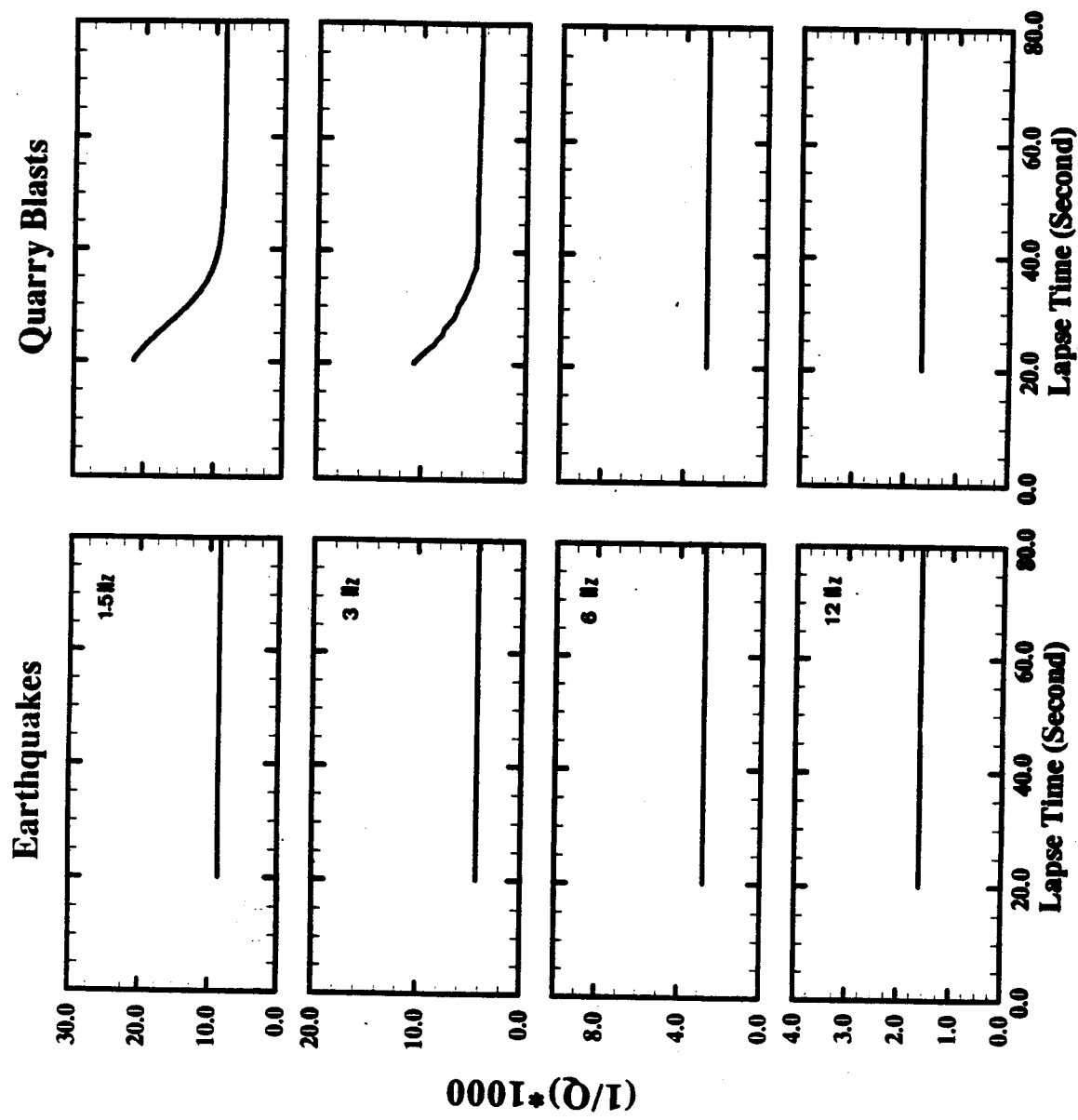


Figure 9: The synthetic coda attenuation curves obtained by solving the energy transfer equations of S and Rayleigh waves, i.e., equations (20a) and (20b). The results correspond to the best fitting coefficients listed in Table 1.

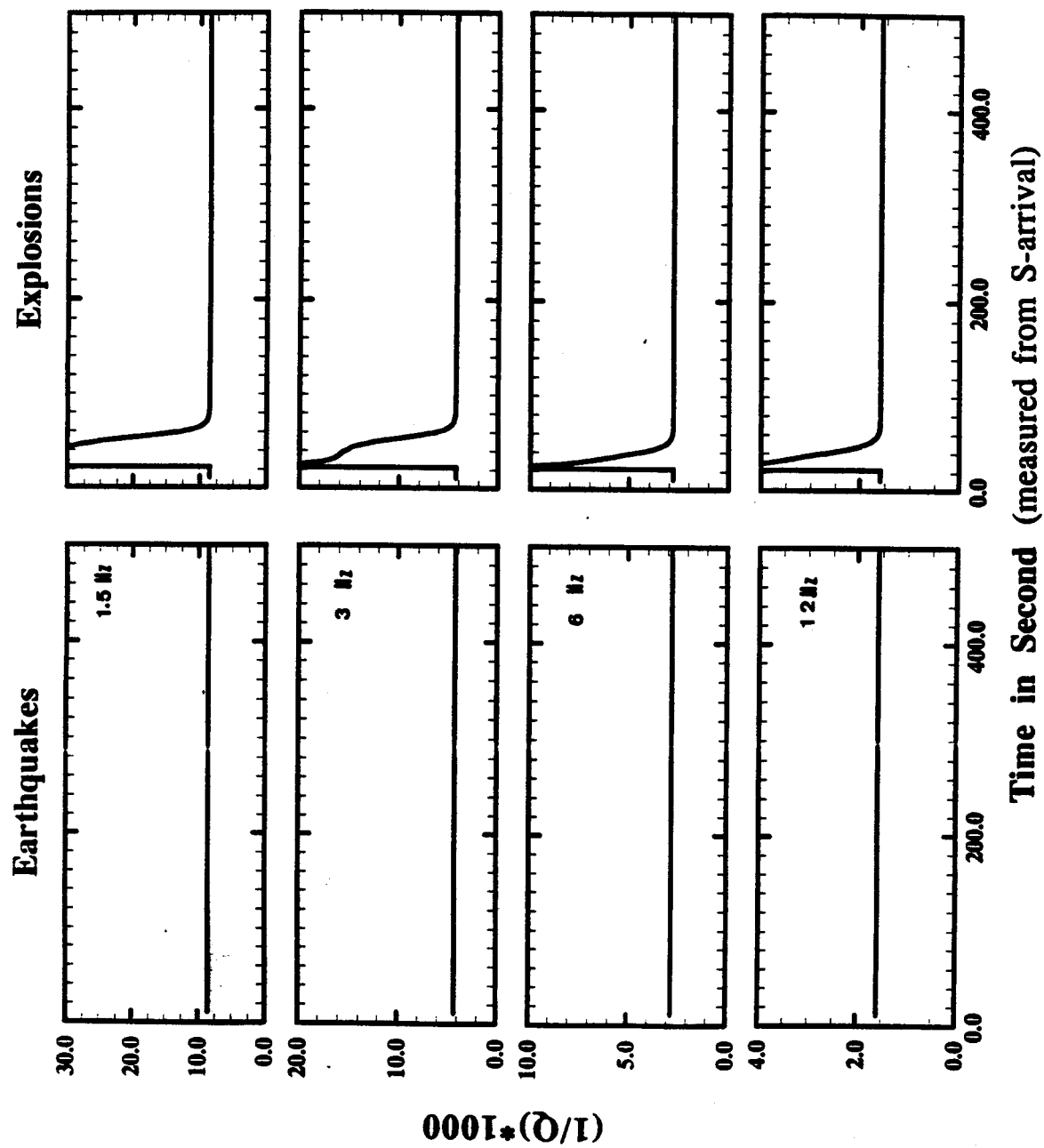


Figure 10: The synthetic coda attenuation curves for the events at regional distance. These results are calculated by assuming the derived various attenuation coefficients and coupling coefficients are still valid in this case.

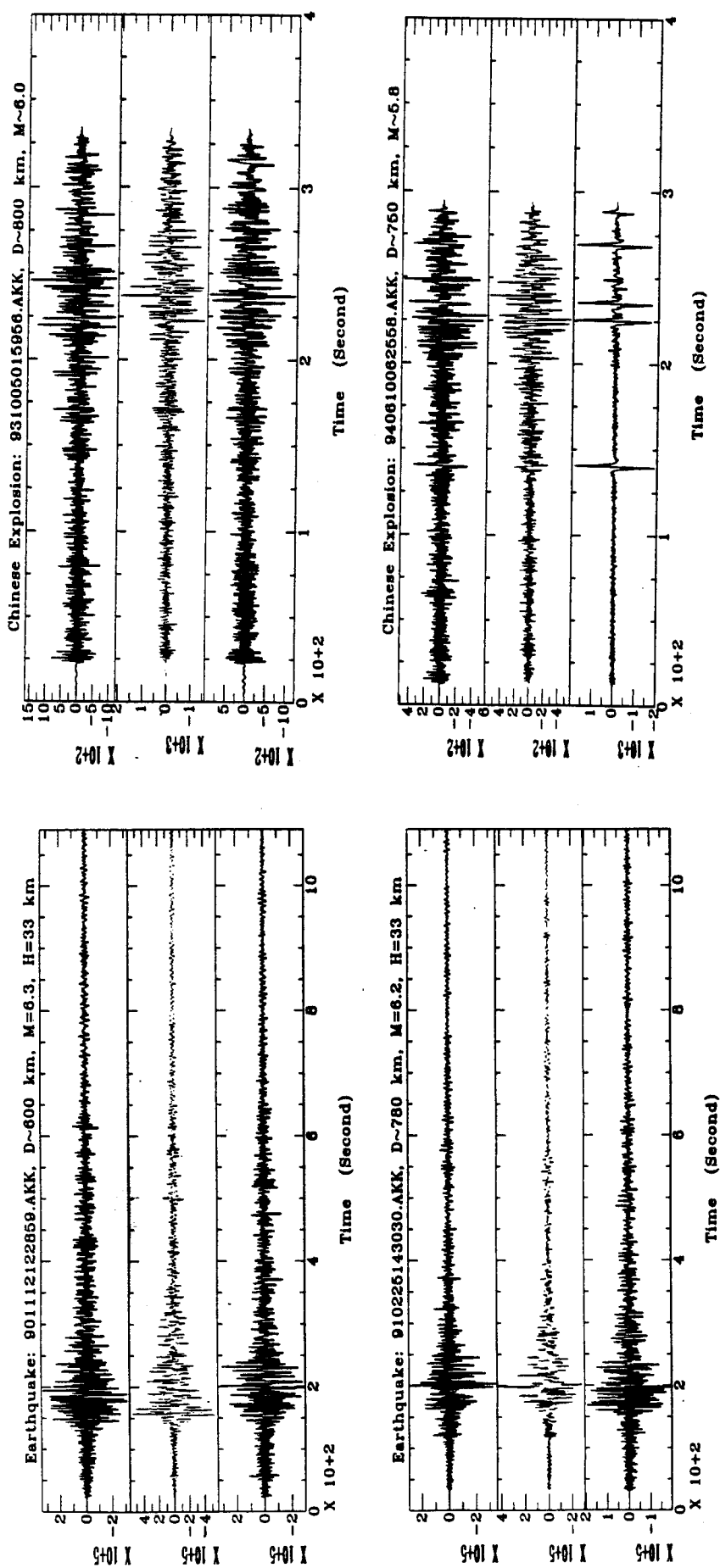


Figure 11: Seismograms of the earthquakes and explosions recorded by CDSN at AKK station.

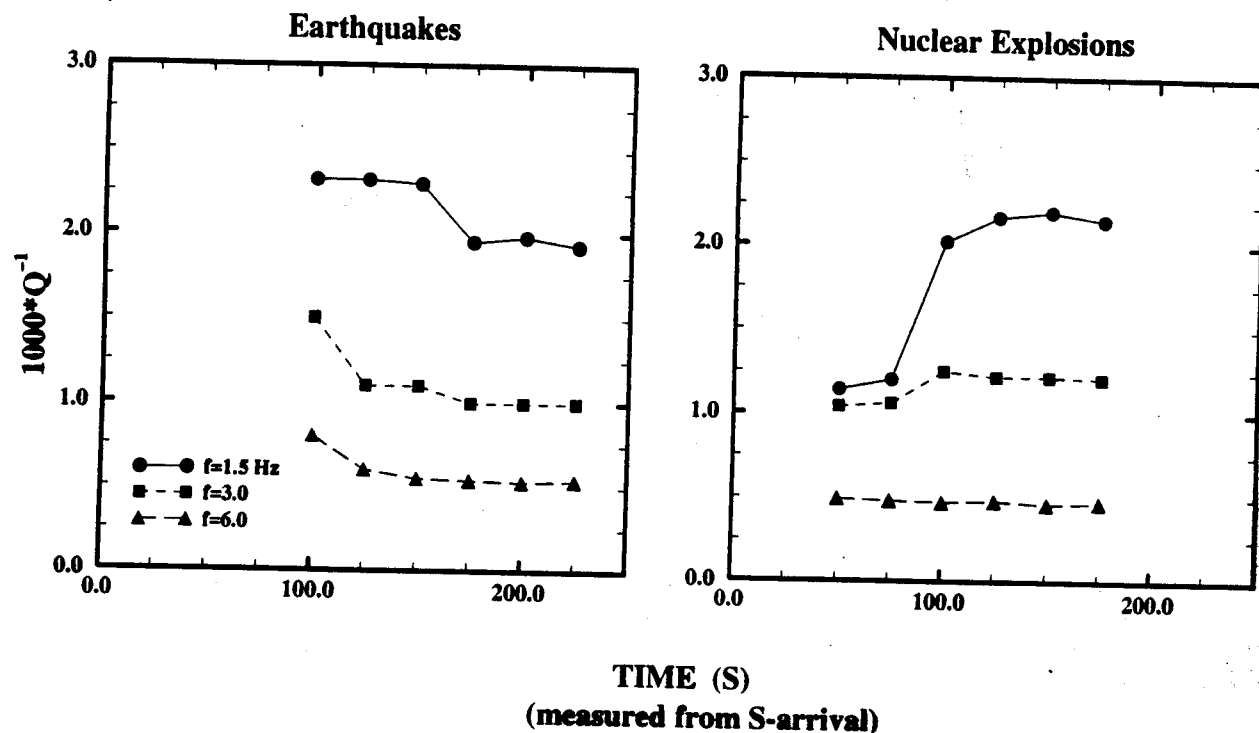


Figure 12 shows the apparent Q^{-1} after S-arrival, for earthquakes and explosions at regional distances, for different frequencies.